Journal of Computational Physics 491 (2023) 112345

Contents lists available at ScienceDirect

Journal of Computational Physics

journal homepage: www.elsevier.com/locate/jcp

Modified multi-phase diffuse-interface model for compound droplets in contact with solid

Junxiang Yang [a], Yibao Li [b], Junseok Kim [c,*]

[a] School of Computer Science and Engineering, Sun Yat-sen University, Guangzhou 510006, China
[b] School of Mathematics and Statistics, Xi'an Jiaotong University, Xi'an 710049, China
[c] Department of Mathematics, Korea University, Seoul, 02841, Republic of Korea

ARTICLE INFO

Article history:
Received 14 October 2022
Received in revised form 22 June 2023
Accepted 2 July 2023
Available online xxxx

Keywords:
Multi-phase system
Diffuse-interface model
Contact angle
Compound droplets

ABSTRACT

In this study, a novel diffuse-interface (phase-field) model is developed to efficiently describe the dynamics of compound droplets in contact with a solid object. Based on a classical four-component Cahn–Hilliard-type system, we propose modified governing equations, in which the solid is represented by an initially fixed phase. By considering Young's equality between surface tensions and microscale contact angles, equilibrium profiles of diffuse interfaces, and horizontal force balance between contact and interfacial angles, a correction term is derived and added into the phase-field equations to reflect the accurate contact line property for each component. The proposed model can be implemented on Eulerian grids in the absence of complicated treatment on the liquid-solid boundary. The standard finite difference method (FDM) is adopted to perform discretization in space. The linear second-order time-accurate method based on the two-step backward differentiation formula (BDF2) and a stabilization technique are adopted to update the phase-field variables. To accelerate convergence in solving the resulting fully discrete system, we use the linear multigrid method. At each time step, the calculations are completely decoupled. The numerical experiments not only indicate the desired accuracy but also show superior capability in complex geometries. Furthermore, the numerical and analytical results for the compound droplets on a flat solid are in good agreement with each other.

1. Introduction

The diffuse-interface (phase-field) method is practical for simulating physical problems such as anti-phase coarsening [1,2], two-phase fluid flows [3–7], vesicle membrane [8–10], and crystallization [11,12]. In many real-world applications, mass-conserved multi-phase physical processes are more common. To investigate multiple interfacial dynamics, various effective models and algorithms based on the Cahn–Hilliard (CH) theory have been proposed (see [13–18] and references therein).

* Corresponding author.
E-mail address: cfdkim@korea.ac.kr (J. Kim).
URL: https://mathematicians.korea.ac.kr/cfdkim/ (J. Kim).

https://doi.org/10.1016/j.jcp.2023.112345
0021-9991/

From [19,20], a typical N-component ($N \geq 3$) CH-type diffuse-interface model is expressed as follows:

$$\frac{\partial \phi_l}{\partial t} = M \Delta \mu_l, \tag{1}$$

$$\mu_l = F'(\phi_l) - \epsilon^2 \Delta \phi_l + \beta(\boldsymbol{\phi}),\ l = 0, 1, ..., N-1, \tag{2}$$

where ϕ_l ($\in [0,1]$) is concentration of l-th component, μ_l is chemical potential, $M > 0$ is constant mobility, $\epsilon > 0$ is a parameter, and $F(\phi_l) = 0.25\phi_l^2(1-\phi_l)^2$. Here, $F'(\phi_l)$ denotes the derivative of $F(\phi_l)$ with respect to ϕ_l. To satisfy the conservative constraint of a multi-component system (i.e., $\phi_0 + \phi_2 + \cdots + \phi_{N-1} = 1$), the simplest choice of Lagrange multiplier is $\beta(\boldsymbol{\phi}) = -\sum_{l=0}^{N-1} F'(\phi_l)/N$ [20]. Because one component in the N-component CH system does not penetrate the bulk phases of the other components, some researchers [21–23] developed a modified ternary CH model to simulate two-phase fluid or material dynamics in irregular domains. To the best of our knowledge, no similar phase-field model exists for treating compound droplets in contact with solids. The main difficulty is the different wetting conditions of compound liquids. Moreover, the contact angles between the droplets and solid substrate are linked to each other through the three-phase interfacial angles between the liquids. To address the contact line problems of ternary fluids in contact with a solid substrate, Zhang et al. [24] defined the contact angle boundary condition in a weighted manner. Subsequently, Huang [25] proposed a similar phase-field lattice Boltzmann method to simulate compound droplets in contact with irregular solids. Recently, Huang et al. [26] investigated the contact angle condition for a second-order phase-field multi-phase flow model. It is worth noting that these methods require artificial treatment on ghost grids near the boundary. To efficiently simulate compound droplets in contact with arbitrary solids, we develop a novel diffuse-interface model based on a modified four-component CH system. One component is initially fixed as a solid phase, and we solve the remaining three components to capture the dynamics of the compound droplets and ambient liquid. By utilizing Young's equality and equilibrium profiles of the phase-field functions, a correction term (penalty term) is added to the original equations to reflect the contact angle condition. Weighted contact angles are designed for each liquid component by considering the horizontal force balance between the contact and interfacial angles. The proposed model is efficient to implement because the calculation is performed on Eulerian grids without explicit treatment on the liquid-solid boundary, that is, we do not need to set the contact angle condition on the domain boundary, and the wetting dynamics is implicitly achieved by solving the governing equations. Furthermore, the proposed model is not limited to the geometrical shape of a solid.

The remainder of this paper is structured as follows. In Section 2, a modified diffuse-interface model with weighted contact angle constraint is derived. The solution algorithms are described in Section 3. Various simulations are conducted in Section 4 to confirm the performance of the proposed model. Section 6 concludes the paper.

2. Modified multi-phase model

Let the solid be represented by a fixed component (i.e., ϕ_0) embedded in the full domain Ω. We assume

$$\phi_0 = \begin{cases} 1, & \text{in Solid,} \\ 0, & \text{otherwise.} \end{cases} \tag{3}$$

It is evident that $0 \leq 1 - \phi_0 \leq 1$ on Ω. Droplets 1 and 2 are represented by ϕ_1 and ϕ_2, respectively, and the ambient liquid is represented by ϕ_3. For compound droplets in contact with the solid, the surface tension coefficients between droplet 1 and solid, droplet 2 and solid, ambient liquid and solid are σ_{01}, σ_{02}, and σ_{03}, respectively. The surface tension coefficients of the liquid interfaces are σ_{13}, σ_{23}, and σ_{12}. Because of the different wetting conditions of the liquids, we define the contact angles as θ_{13}, θ_{23}, θ_{12}, and θ_{21}. Clearly, we have $\theta_{21} = 180^\circ - \theta_{12}$. It is worth noting that the local flatness of the solid surface is assumed in this study. In future work, we will further consider an approach for handling rough surfaces with sharp corners. At the ternary contact point, the interfacial angles are ψ_1, ψ_2, ψ_3, and $\psi_1 + \psi_2 + \psi_3 = 360^\circ$. From the balance of interfacial angles at the equilibrium state, we have

$$\frac{\sin\psi_1}{\sigma_{23}} = \frac{\sin\psi_2}{\sigma_{13}} = \frac{\sin\psi_3}{\sigma_{12}}. \tag{4}$$

Fig. 1 shows a schematic illustration of compound droplets in contact with a solid substrate.

On the liquid-solid boundary, the relationship between the contact and surface tension coefficients is expressed by Young's equality

$$\sigma_{pq}\cos\theta_{pq} = \sigma_{0q} - \sigma_{0p}. \tag{5}$$

Here, the subscripts p and q can be 1, 2, 3, and $p \neq q$. By considering the horizontal force balance [24], the following relation can be derived from Eqs. (4) and (5)

$$\sin\psi_2\cos\theta_{13} - \sin\psi_3\cos\theta_{12} - \sin\psi_1\cos\theta_{23} = 0. \tag{6}$$

This equality indicates that the contact and interfacial angles are linked to each other. With any two contact angles and presupposed interfacial forces, the wetting condition of compound droplets can be uniquely determined. Under the equilibrium

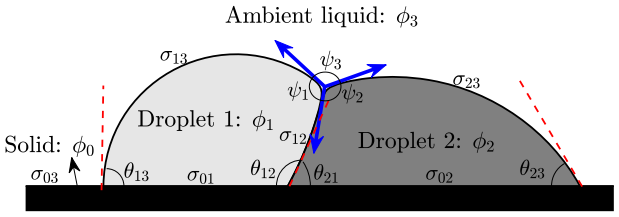

Fig. 1. Schematic illustration of compound droplets in contact with solid.

profile of a phase-field function [20], we know that $|\nabla\phi_l| = \phi_l(1-\phi_l)/(\sqrt{2}\epsilon)$ holds approximately. Let $\tilde{\theta}$ be an equivalent contact angle, Young's equality leads to

$$\nabla\phi_l \cdot \mathbf{n} = |\nabla\phi_l|\cos\tilde{\theta} = -\phi_l(\phi_l-1)\cos\tilde{\theta}/(\sqrt{2}\epsilon), \tag{7}$$

where $\mathbf{n} = \nabla\phi_0/|\nabla\phi_0|$ denotes the unit normal vector to the solid. By recasting Eq. (7), we derive the following equality

$$\epsilon^2\nabla\phi_0\cdot\nabla\phi_l + \epsilon\phi_l(\phi_l-1)|\nabla\phi_0|\cos\tilde{\theta}/\sqrt{2} = 0. \tag{8}$$

By taking the droplet 1 as an example, it can be observed that the equivalent contact angle $\tilde{\theta}$ can be either θ_{13} or θ_{12}. This is a typical difference from the contact angle in a two-phase system (single droplet) contacting a solid because we need to consider a possible angle at each spatial point. Similar problems should also be considered for droplet 2 and ambient liquid. Inspired by [24], we present weighted contact angles as follows

$$\theta_1 = \frac{\phi_3}{\phi_2+\phi_3}\theta_{13} + \frac{\phi_2}{\phi_2+\phi_3}\theta_{12}, \tag{9}$$

$$\theta_2 = \frac{\phi_3}{\phi_1+\phi_3}\theta_{23} + \frac{\phi_1}{\phi_1+\phi_3}\theta_{21}. \tag{10}$$

For droplets 1 and 2, we replace the equivalent contact angle $\tilde{\theta}$ in Eq. (8) by θ_1 and θ_2, respectively. Because the weighted contact angles are determined by local phase-field functions, an accurate contact angle at each spatial point can be easily achieved. To avoid the bias phenomenon at the liquid-solid-liquid contact point [27], we successively update ϕ_1, ϕ_2, and ϕ_3 in this study. To accurately evaluate the contact angle of the ambient liquid, we propose the following weighted angle

$$\theta_3 = 180^\circ - \left(\frac{\phi_1}{\phi_1+\phi_2}\theta_1 + \frac{\phi_2}{\phi_1+\phi_2}\theta_2\right). \tag{11}$$

For the ambient liquid, we replace the equivalent contact angle $\tilde{\theta}$ in Eq. (8) by θ_3. By adding Eq. (8) into Eq. (2) and neglecting the small effect from $\epsilon^2\phi_0\Delta\phi_l$ in liquid regions, the modified diffuse-interface model can be expressed as

$$\frac{\partial\phi_l}{\partial t} = M\nabla\cdot((1-\phi_0)\nabla\mu_l), \tag{12}$$

$$\mu_l = F'(\phi_l) + \hat{\beta}(\boldsymbol{\phi}) + \epsilon\phi_l(\phi_l-1)|\nabla\phi_0|\cos\theta_l/\sqrt{2} - \epsilon^2\nabla\cdot((1-\phi_0)\nabla\phi_l),\ l=1,2,3, \tag{13}$$

where ϕ_0 is fixed during the initial stage. Inspired by the diffuse-domain (DD) method [28], we multiply $F'(\phi_l)$ with $1-\phi_0$ and rewrite Eqs. (12) and (13) to be

$$\frac{\partial\phi_l}{\partial t} = M\nabla\cdot((1-\phi_0)\nabla\mu_l), \tag{14}$$

$$\mu_l = (1-\phi_0)F'(\phi_l) + \tilde{\beta}(\boldsymbol{\phi}) + \epsilon\phi_l(\phi_l-1)|\nabla\phi_0|\cos\theta_l/\sqrt{2} - \epsilon^2\nabla\cdot((1-\phi_0)\nabla\phi_l),\ l=1,2,3. \tag{15}$$

To satisfy the conservative constraint (i.e., $\sum_{l=0}^{3}\phi_l = 1$), the modified version of the Lagrange multiplier is

$$\tilde{\beta}(\boldsymbol{\phi}) = -\frac{1}{3}\left[\sum_{l=1}^{3}\left((1-\phi_0)F'(\phi_l) + \epsilon\phi_l(\phi_l-1)|\nabla\phi_0|\cos\theta_l/\sqrt{2}\right)\right].$$

In Appendices A and B, we provide some details of the derivation of Eq. (13) and a specific form of $\tilde{\beta}(\boldsymbol{\phi})$. Each component is calculated in the full domain without explicit treatment of the boundary condition. The wetting phenomenon is achieved implicitly by updating the governing equations. On the boundary of the full domain, we can consider simple natural boundary conditions such as the homogeneous Neumann condition or periodic condition.

Remark 2.1. Based on the geometrical relation and equilibrium assumption of the interface, we derive the governing equations for modeling wetting problems on a locally flat surface. We note that the present phase-field model is not derived from a free energy functional based on gradient flow theory. Moreover, the weighted contact angle θ_l $(l = 1, 2, 3)$ is related to phase function ϕ_l. It is difficult to construct an energy functional using Eqs. (12) and (13). Therefore, we conclude that the proposed model does not correspond to an energy law.

3. Solution algorithm

Let $\Delta t = T/N_T$ be the time step, where T is the total time and N_T is the number of time iterations. Based on the second-order backward difference formula (BDF2) over time, the temporal discrete equations in Eqs. (14) and (15) are expressed as

$$\frac{3\phi_l^{n+1} - 4\phi_l^n + \phi_l^{n-1}}{2\Delta t} = M\nabla\cdot((1-\phi_0)\nabla\mu_l^{n+1}), \tag{16}$$

$$\begin{aligned}\mu_l^{n+1} &= (1-\phi_0)F'(\phi_l^*) + \tilde{\beta}(\boldsymbol{\phi}^*) + \epsilon\phi_l^*(\phi_l^*-1)|\nabla\phi_0|\cos\theta_l^*/\sqrt{2}\\ &\quad - \epsilon^2\nabla\cdot((1-\phi_0)\nabla\phi_l^{n+1}) + S(\phi_l^{n+1} - \phi_l^*),\end{aligned} \tag{17}$$

where $l = 1, 2, 3$ and $(\cdot)^* = 2(\cdot)^n - (\cdot)^{n-1}$ is the extrapolation. The stabilization term (last term) in Eq. (17) is used to improve the stability and $S > 0$ is a constant. The equations are discretized in space using the finite difference method (FDM). The phase-field functions ϕ_l, $l = 0, 1, 2, 3$ are stored at the cell centers. Before the start of the fully discrete scheme, we define some useful notations in a two-dimensional (2D) space. The extension to three-dimensional (3D) space follows a similar approach. The computational domain is $\Omega = (L_x, R_x)\times(B_y, T_y)$. The uniform mesh size (space step) is $h = (R_x - L_x)/N_x = (T_y - B_y)/N_y$, where N_x and N_y are even positive integers. The set of cell centers in the full domain is defined as $\Omega_d = \{(x_i, y_j)|x_i = L_x + (i-0.5)h,\ \ y_j = B_y + (j-0.5)h\}$, where $1 \le i \le N_x$ and $1 \le j \le N_y$. Let $\phi_{l,ij}^n = \phi_l(x_i, y_j, n\Delta t)$, $\mu_{l,ij}^n = \mu_l(x_i, y_j, n\Delta t)$, and $\phi_{0,ij} = \phi_0(x_i, y_j)$. The fully discrete scheme is written as

$$\frac{3\phi_{l,ij}^{n+1} - 4\phi_{l,ij}^n + \phi_{l,ij}^{n-1}}{2\Delta t} = M\nabla_d\cdot((1-\phi_{0,ij})\nabla_d\mu_{l,ij}^{n+1}), \tag{18}$$

$$\begin{aligned}\mu_{l,ij}^{n+1} &= (1-\phi_{0,ij})F'(\phi_{l,ij}^*) + \tilde{\beta}(\boldsymbol{\phi}^*{}_{ij}) + \epsilon\phi_{l,ij}^*(\phi_{l,ij}^*-1)|\nabla_h\phi_{0,ij}|\cos\theta_{l,ij}^*/\sqrt{2}\\ &\quad - \epsilon^2\nabla_d\cdot((1-\phi_{0,ij})\nabla_d\phi_{l,ij}^{n+1}) + S(\phi_{l,ij}^{n+1} - \phi_{l,ij}^*),\ l = 1, 2, 3,\end{aligned} \tag{19}$$

where

$$\nabla_h\phi_{0,ij} = \left(\frac{\phi_{0,i+1,j} - \phi_{0,i-1,j}}{2h}, \frac{\phi_{0,i,j+1} - \phi_{0,i,j-1}}{2h}\right).$$

For simplicity, we let $\mathcal{M}_{ij} = 1 - \phi_{0,ij}$. The discrete divergence term is defined as follows:

$$\begin{aligned}\nabla_d\cdot(\mathcal{M}_{ij}\nabla_d\mu_{l,ij}) &= \frac{\mathcal{M}_{i+\frac{1}{2},j}(\mu_{l,i+1,j} - \mu_{l,ij}) - \mathcal{M}_{i-\frac{1}{2},j}(\mu_{l,ij} - \mu_{l,i-1,j})}{h^2}\\ &\quad + \frac{\mathcal{M}_{i,j+\frac{1}{2}}(\mu_{l,i,j+1} - \mu_{l,ij}) - \mathcal{M}_{i,j-\frac{1}{2}}(\mu_{l,ij} - \mu_{l,i,j-1})}{h^2},\end{aligned}$$

where $\mathcal{M}_{i+\frac{1}{2},j} = 0.5(\mathcal{M}_{i+1,j} + \mathcal{M}_{ij})$ and the other quantities are similarly defined. This definition is also used for $\nabla_d\cdot(\mathcal{M}_{ij}\nabla_d\phi_{l,ij})$. On the boundary of Ω_d, we consider periodic or the following discrete homogeneous Neumann boundary conditions

$$\begin{aligned}&\phi_{l,0,j} = \phi_{l,1,j},\quad \phi_{l,N_x+1,j} = \phi_{l,N_x,j},\quad \phi_{l,i,0} = \phi_{l,i,1},\quad \phi_{l,i,N_y+1} = \phi_{l,i,N_y},\\ &\mu_{l,0,j} = \mu_{l,1,j},\quad \mu_{l,N_x+1,j} = \mu_{l,N_x,j},\quad \mu_{l,i,0} = \mu_{l,i,1},\quad \mu_{l,i,N_y+1} = \mu_{l,i,N_y},\ l = 1, 2, 3.\end{aligned}$$

To accelerate convergence, we use the linear multigrid method [29] to solve the resulting discrete system. The algorithms are briefly introduced as follows. Equations (18) and (19) are recast to be

$$L_d(\phi_l^{n+1}, \mu_l^{n+1}) = (s_a^n, s_b^n), \tag{20}$$

where the linear operator L_d is

$$L_d(\phi_l^{n+1}, \mu_l^{n+1}) = \left(\frac{3\phi_{l,ij}^{n+1}}{2\Delta t} - M\nabla_d\cdot((1-\phi_{0,ij})\nabla_d\mu_{l,ij}^{n+1}),\ \mu_{l,ij}^{n+1} + \epsilon^2\nabla_d\cdot((1-\phi_{0,ij})\nabla_d\phi_{l,ij}^{n+1}) - S\phi_{l,ij}^{n+1}\right),$$

and the source terms are as follows:

$$s_a^n = \frac{4\phi_{l,ij}^n - \phi_{l,ij}^{n-1}}{2\Delta t},$$
$$s_b^n = (1-\phi_{0,ij})F'(\phi_{l,ij}^*) + \tilde{\beta}(\boldsymbol{\phi}^*{}_{ij}) + \epsilon\phi_{l,ij}^*(\phi_{l,ij}^*-1)|\nabla_h\phi_{0,ij}|\cos\theta_{l,ij}^*/\sqrt{2} - \epsilon^2\nabla_d\cdot((1-\phi_{0,ij})\nabla_d\phi_{l,ij}^{n+1}) - S\phi_{l,ij}^*.$$

The multigrid algorithm with a V-cycle [29–31] can be summarized as follows:

$$\left(\phi_{l,k}^{n+1,m+1}, \mu_{l,k}^{n+1,m+1}\right) = \text{V-cycle}\left(k, \phi_{l,k}^{n+1,m}, \mu_{l,k}^{n+1,m}, L_d, s_a^n, s_b^n, \nu_a, \nu_b\right), \tag{21}$$

where subscript k indicates the approximation on a mesh grid Ω_k containing $2^k \times 2^k$ grids. Here, k is the multigrid level. The superscripts $m+1$ and m indicate the results obtained after and before one V-cycle, respectively. In one V-cycle, we successively perform the pre-smoothing, coarse grid correction, and post-smoothing steps as follows:

Pre-smoothing.

$$\left(\bar{\phi}_{l,k}^{n+1,m}, \bar{\mu}_{l,k}^{n+1,m}\right) = \text{SMOOTH}^{\nu_a}\left(\phi_{l,k}^{n+1,m}, \mu_{l,k}^{n+1,m}, L_d, s_a^n, s_b^n\right), \tag{22}$$

where $(\bar{\phi}_{l,k}^{n+1,m}, \bar{\mu}_{l,k}^{n+1,m})$ are the updated results after ν_a iterations.

Coarse grid correction.

1. Calculate the defects: $(\bar{d}_{a,k}^m, \bar{d}_{b,k}^m) = (s_a^n, s_b^n) - L_d\left(\bar{\phi}_{l,k}^{n+1,m}, \bar{\mu}_{l,k}^{n+1,m}\right)$.
2. Restrict the defects: $\bar{d}_{a,k-1}^m = I_k^{k-1}\bar{d}_{a,k}^m, \quad \bar{d}_{b,k-1}^m = I_k^{k-1}\bar{d}_{b,k}^m$.
3. If $k > 1$, we solve the discrete system on a coarser grid Ω_{k-1} using the initial conditions $(0,0)$ and source terms $(\bar{d}_{a,k-1}^m, \bar{d}_{b,k-1}^m)$. Otherwise, we calculate the solutions using a smoothing step.
4. Interpolate the correction: $\hat{u}_{a,k}^{n+1} = I_{k-1}^k\hat{u}_{a,k-1}^{n+1,m}, \quad \hat{u}_{b,k}^{n+1} = I_{k-1}^k\hat{u}_{b,k-1}^{n+1,m}$.
5. Calculate the approximations on Ω_k:

$$\left(\tilde{\phi}_{l,k}^{n+1,m}, \tilde{\mu}_{l,k}^{n+1,m}\right) = \left(\bar{\phi}_{l,k}^{n+1,m}, \bar{\mu}_{l,k}^{n+1,m}\right) + \left(\hat{u}_{a,k}^{n+1,m}, \hat{u}_{b,k}^{n+1,m}\right). \tag{23}$$

Post-smoothing.

$$\left(\phi_{l,k}^{n+1,m+1}, \mu_{l,k}^{n+1,m+1}\right) = \text{SMOOTH}^{\nu_b}\left(\tilde{\phi}_{l,k}^{n+1,m}, \tilde{\mu}_{l,k}^{n+1,m}, L_d, s_a^n, s_b^n\right). \tag{24}$$

Please refer to [29–31] for more details regarding the multigrid algorithm.

Remark 3.1. In the present study, we design a temporally second-order accurate scheme based on the BDF2. Note that BDF2-type method requires information from the previous time levels. To initiate the algorithm, the first-order backward Euler method is used to perform calculations in the first-time step. Our proposed model can also be discretized in time by using other approaches such as the Crank–Nicolson and Runge–Kutta-type methods.

4. Numerical validations

This section presents several computational experiments to validate the accuracy and capability of the proposed method. The parameters are set to $M = 1$ and $S = 2$ in the tests. Without specific requirement, the full computational domain is $\Omega = (0,4)\times(0,2)$ and mesh size is $h = 1/128$.

4.1. Convergence tests

The initial settings are shown in Fig. 2(a). To test the accuracy in terms of time, the reference solutions are calculated using a smaller time step $\delta t = 0.001h^2$. The increasingly coarser time steps ($\Delta t = 8\delta t$, $16\delta t$, $32\delta t$, and $64\delta t$) are used to compute the convergence rate. The computational results shown in Table 1 indicate that the second-order accuracy in time is achieved. To test the accuracy in terms of space, the reference solutions are obtained using a finer mesh size (i.e., $h = 1/256$). The time step is fixed as $\Delta t = 6.10\text{e-}8$ and $\epsilon = 0.06$. The increasingly coarser mesh sizes ($h = 1/128$, $1/64$, and $1/32$) are used. For the definitions of discrete L^2-errors and the convergence rate, see [32]. From the numerical results plotted in Table 2, we observe that the algorithm has a second-order accuracy in terms of space.

4.2. Compound droplets on a flat substrate

In [24], Zhang et al. presented analytical expressions for the spreading lengths of compound droplets on a substrate. To simulate different wetting phenomena, they proposed a weighted contact angle condition on the bottom boundary of a regular domain. It is worth emphasizing that our proposed model does not need to directly handle the boundary conditions,

Table 1
L^2-errors and convergence rates for ϕ_1 and ϕ_2 with respect to different time steps.

Δt	$64\delta t$		$32\delta t$		$16\delta t$		$8\delta t$
Error for ϕ_1:	1.60e-3		4.53e-4		1.06e-4		2.86e-5
Rate for ϕ_1:		1.82		2.09		1.89	
Error for ϕ_2:	1.60e-3		4.53e-4		1.04e-4		2.57e-5
Rate for ϕ_2:		1.82		2.13		2.01	

Table 2
L^2-errors and convergence rates for ϕ_1 and ϕ_2 with respect to different mesh sizes.

Mesh size:	1/32		1/64		1/128
Error for ϕ_1:	2.39e-2		5.80e-3		1.20e-3
Rate for ϕ_1:		2.04		2.27	
Error for ϕ_2:	2.28e-2		5.60e-3		1.20e-3
Rate for ϕ_2:		2.03		2.22	

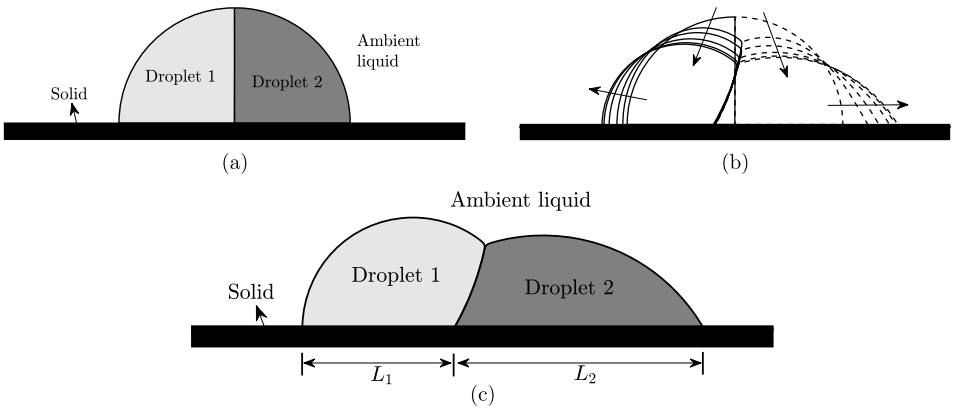

Fig. 2. Compound droplets on a flat substrate. The initial state and evolution process are displayed in (a) and (b). Here, the arrows indicate the directions of evolution. The steady state is shown in (c).

Table 3
Exact and numerical results of contact angles: θ_{13}, θ_{23}, θ_{12}, and θ_{21}.

Contact angle:	θ_{13}	θ_{23}	θ_{12}	θ_{21}
Exact value:	90°	60°	120°	60°
Numerical value:	90.6°	60.4°	120.3°	59.7°

Table 4
Analytical and numerical results of spreading lengths and their relative errors. Here, $\Delta t = 0.1$ is used.

Length: L_1	L_2	
Analytical value:	1.072	1.707
Numerical value:	1.0643	1.6929
Relative error:	0.72%	0.83%

and different wetting conditions can be implicitly achieved by solving the governing equations. In the present simulation, the region ($y < 0.15$) is occupied by a solid phase (i.e., ϕ_0), the compound droplets are located at $(2, 0.15)$ and have the same area $0.25\pi R^2$, where $R = 1$ is the radius. The initial conditions are shown in Fig. 2(a). We set $\Delta t = 0.1$, $h = 4/512 = 0.0078$, $\epsilon = 9.4\text{e-}3$, $\theta_{13} = 90°$, $\theta_{23} = 60°$, $\theta_{12} = 120°$, and $\theta_{21} = 180° - \theta_{12}$, which corresponds to $\psi_1 = \psi_2 = \psi_3 = 120°$. The time evolutions of droplets 1 (solid line) and 2 (dashed line) are shown in Fig. 2(b). The steady state is displayed in Fig. 2(c). Table 3 lists the exact and numerical values of the contact angles θ_{13}, θ_{23}, θ_{12}, and θ_{21}. The spreading lengths and relative errors are listed in Table 4. Please refer to [24] for the calculation of analytical spreading lengths. It can be seen that the computational and analytical results are quantitatively similar. The relative errors are less than 1%.

To show the convergence with respect to ϵ, we consider the same simulation with unchanged parameters except the increasingly smaller values of ϵ: 6.60e-3, 1.32e-2, and 2.64e-2. The analytical spreading state in [24] is considered as a

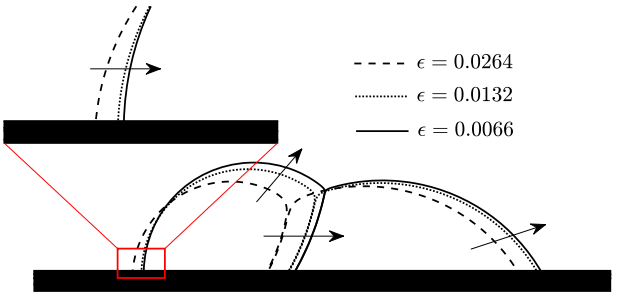

Fig. 3. Convergence of interface profile with respect to different values of ϵ.

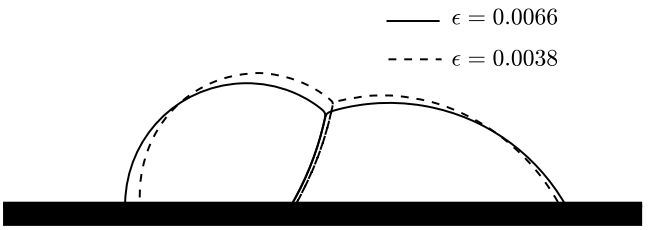

Fig. 4. Spreading states at $t = 500$ with respect to different values of ϵ.

reference. In Fig. 3, the interface profiles with respect to different ϵ values are plotted. Here, the inset shows the local close-up view. As the refinement of ϵ, we observe the convergence of interface profile.

The diffuse-interface method analytically approximates the sharp interface model as a decrease in ϵ. However, too small value of ϵ will lead to the pinning phenomenon of interfacial dynamics. To verify this, we perform the simulation with a smaller value of ϵ. Fig. 4 plots the final stages ($t = 500$) with respect to $\epsilon = 6.60\text{e-}3$ and $3.80\text{e-}3$. The result indicates that a smaller ϵ is not adoptable in present mesh size because the evolutions of the compound droplets are delayed. For this present benchmark problem, $\epsilon = 6.60\text{e-}3$ is an appropriate choice.

Remark 4.1. With sufficiently small mesh size, the diffuse-interface model can converge as the value of ϵ is appropriately refined. However, too small value of ϵ requires fine enough spatial grid size to numerically resolve the interfacial transition layer. Otherwise, the numerical pinning effect may occur, leading to undesired results. In practice, the number of grid points across the interfacial transition layer should be larger than 4 to ensure that the Laplacian operator can be accurately calculated using a finite difference stencil. To approximate the sharp interface result, on can use the adaptive mesh refinement technique [33] to efficiently increase the grid points in interfacial transition layer.

4.3. Effect of stabilization parameter

In Eq. (19), we introduce a stabilization term to improve the stability. It is worth noting that the stabilization technique has been extensively adopted for designing linear and stable time-marching schemes for phase-field problems. In a pioneering study, Shen and Yang [34] developed a linear and unconditionally stable scheme for the Allen–Cahn (AC) equation. To obtain the desired stability, they introduced a stabilization term and clarified the value of the stabilization parameter via energy-stable condition. Yang and Kim [35] numerically investigated the effect of the stabilization parameter on the energy of square crystal pattern on a sphere. In recent years, stabilization idea has been successfully used in various auxiliary variable-type methods, such as the invariant energy quadratization (IEQ) method [36] and the scalar auxiliary variable (SAV) method [37]. To test the effect of S, we simulate compound droplets in contact with a flat substrate with $\Delta t = 0.1$, $h = 4/512 = 0.0078$, $\epsilon = 0.0094$, and $M = 1$. Fig. 5 shows the computational results at $t = 0.2$ with $S = 0$ and $S = 2$. With $S = 0$, the stabilization term is absent and we observe that the computation blows up. By contrast, $S = 2$ leads to stable results. As shown in Fig. 2, the computation with $S = 2$ remains stable even if the relatively steady state reaches. As reported by [38,39], an excessively large value of S introduces additional errors. Therefore, we empirically choose $S = 2$ in all the simulations.

It is worth noting that $S = 2$ has been extensively used in previous works [34,36,37] to satisfy the energy estimation of phase-field models. For a linear semi-implicit scheme, the stabilization term improves the stability but may delay the evolutional dynamics. It is better to perform an accurate simulation with a relatively smaller value of S and a finer time step. In present study, we find that $S = 2$ does not delay the evolutional dynamics. To confirm this, the aforementioned test is performed with the same parameters except a smaller stabilization parameter $S = 0.6$ and a finer time step $\Delta t = 0.01$. In Fig. 6, highly consistent phase profiles at specific moments can be observed. Here, the reference is set to a numerical result with $S = 2$ and a larger time step. This comparison test indicates that $S = 2$ has almost no effect on the dynamics because

Fig. 5. Snapshots of compound droplets in contact with a flat substrate with respect to $S = 0$ and $S = 2$.

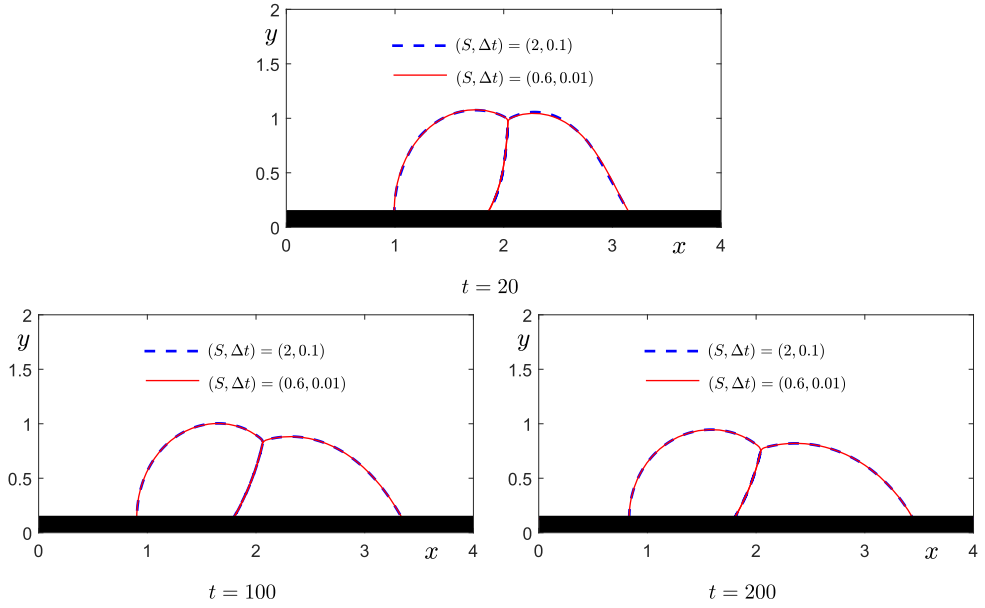

Fig. 6. Spreading states of compound droplets with respect to different values of S and time steps. The computational moments are shown under each figure.

the analytical and numerical results under different time steps and different stabilization parameters are in good agreement. It is still worth noting that the difference at $t = 20$ appears noticeably larger than the differences at $t = 100$ and $t = 200$, although all of them are relatively small.

4.4. Compound droplets on a rough substrate

Contact angle hysteresis is a common physical phenomenon. The real contact angle is generally not equal to the presupposed value, because Young's equality does not hold on the rough surface. To simulate this, we consider a rough substrate with periodic wave structures, as shown in Fig. 7(a). The parameters are the same as those described in the previous subsection. Fig. 7 displays snapshots at the final stage ($t = 500$) in which the inset shows the local close-up view. We observe that the computed contact angle between droplet 2 and solid slightly deviates from its desired value. In the present simulation, we note that the contact angle is still measured on a local macroscopic flat surface. For a real physical problem, the microscopic contact angle should be considered. Young's equality is modified as follows:

$$\sigma_{pq} \cos\theta_{pq} + \frac{\tau}{r_B} = \sigma_{0q} - \sigma_{0p}, \tag{25}$$

where τ is the linear tension from thermodynamics and r_B is the effective radius of a droplet in contact with the solid. The present study only aims to develop a phase-field approach for modeling the wetting problem on an ideal surface with flatness, and an extended model for microscopic contact angle on real rough surfaces will be further studied in our future work.

4.5. Compound droplets on a tilted substrate

Here, we investigate the evolution of the compound droplets on a tilted substrate. The computational domain is $\Omega = (0, 4) \times (0, 2)$. The solid phase occupies the region locating under the tilted line through point $(2, 0.15)$. A compound droplet with the same initial area as in subsection 4.2 is set on the tilted substrate. To perform the comparison, we calculate the compound droplets in a regular domain using a method similar to that in [24] and then rotate the results at a specific angle.

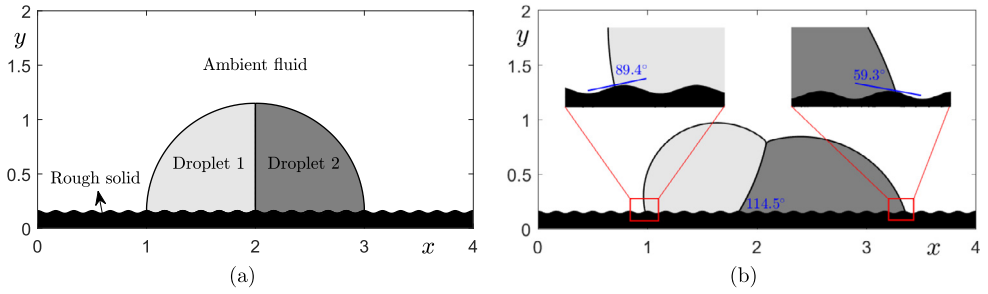

Fig. 7. Compound droplets on a rough substrate. The initial and final states are shown in (a) and (b), respectively.

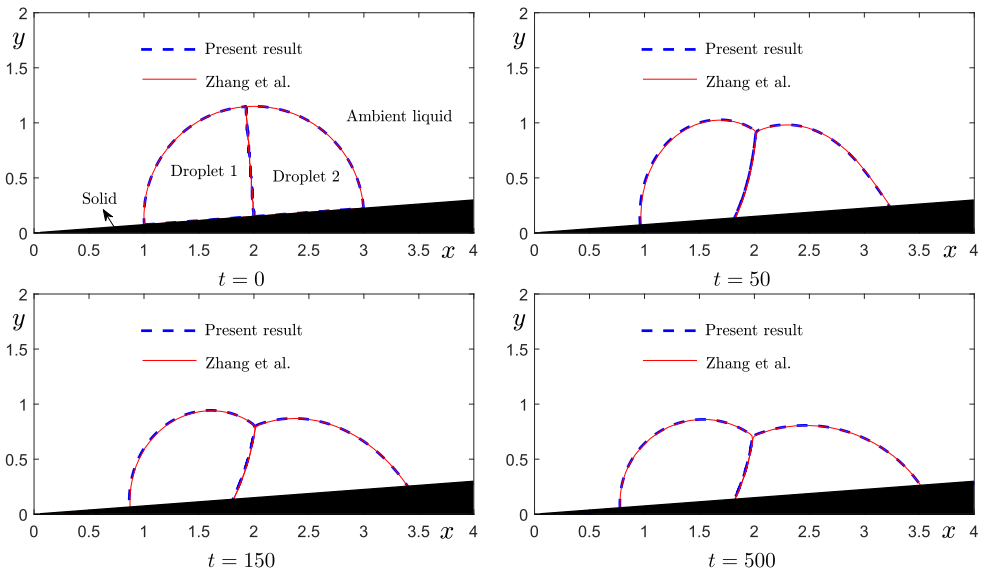

Fig. 8. Compound droplets on a tilted substrate. The results computed by the proposed and previous methods are represented by the solid line and open circle, respectively. Under each figure, the computational moment is shown.

Fig. 8 shows the comparisons at different moments. We can observe that the computational results are in good agreement with each other.

4.6. Compound droplets on the circular solid

To demonstrate the capability of our proposed mathematical model on a curved surface, we initially define compound droplets with radius $R = 0.7$ near a circular solid, which is similar to the setting in [25]. The entire computational domain is $\Omega = (0, 4) \times (0, 4)$, $h = 1/64$, and $\Delta t = 0.1$. In the first case, a circular solid with radius $R_s = 0.6$ is located at $(2, 1.4)$. The contact angles are $\theta_{13} = 90°$, $\theta_{23} = 45°$, $\theta_{12} = 135°$, and $\theta_{21} = 180° - \theta_{12}$, corresponding to $\psi_1 = \psi_2 = \psi_3 = 120°$. The final stage is shown in Fig. 9(a). In the second case, the radius of solid is $R_s = 0.8$. The contact angles are $\theta_{13} = 120°$, $\theta_{23} = 69.295°$, $\theta_{12} = 135°$, and $\theta_{21} = 180° - \theta_{12}$, which correspond to $\psi_1 = 135°, \psi_2 = 120°, \psi_3 = 105°$. Fig. 9 shows the results at $t = 500$. The present computational results are qualitatively similar to the previous results in [25].

In Fig. 10(a) and (b), we plot $\left|\sum_{l=0}^{3} \phi_l - 1\right|$ at final stage ($t = 500$) with respect to cases 1 and 2, respectively. It can be observed that the local relative errors are close to zero. For the CH-type phase field model, it is well known that the order parameter cannot be precisely bounded by 0 and 1. Furthermore, Lee and Kim [20] reported that the spurious phases may appear for most Lagrange multipliers. These two reasons likely results in the value of $\left|\sum_{l=0}^{3} \phi_l - 1\right|$ not being strictly zero. In our upcoming works, we plan to investigate a more accurate multi-phase model with interfacial correction and a new component-dependent Lagrange multiplier to further improve the accuracy of the simulation.

Next, we perform similar simulations in 3D space. A spherical solid with radius 0.8 and center position $(2, 2, 1.1)$ is embedded into the entire computational domain $\Omega = (0, 4) \times (0, 4) \times (0, 4)$. The initial compound droplets with a radius of 0.9 are located at $(2, 2, 2.35)$. In the first case, we set $\theta_{13} = 90°$, $\theta_{23} = 45°$, $\theta_{12} = 135°$. In the second case, we set $\theta_{13} = 120°$, $\theta_{23} = 69.295°$, $\theta_{12} = 135°$. The left and right columns in Fig. 11 show the computational results with respect to cases 1 and

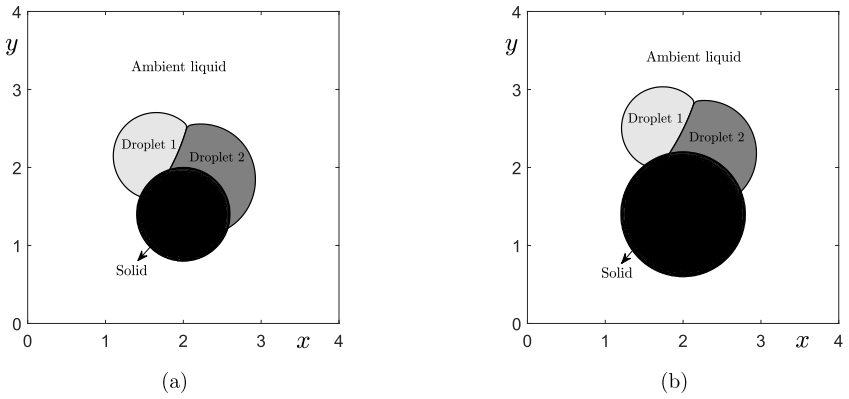

Fig. 9. Compound droplets on the circular solid. The results corresponding to the first and second cases are shown in (a) and (b), respectively. The summations of average concentrations are plotted in (c).

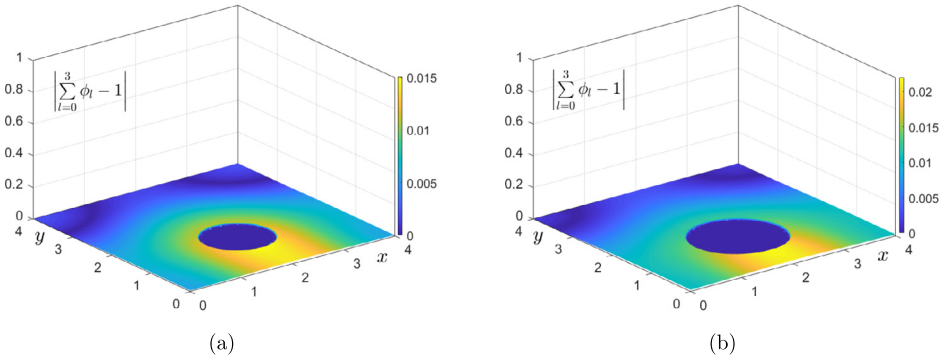

Fig. 10. Local relative error $\left|\sum_{l=0}^{3}\phi_l - 1\right|$ at final stage with respect to case 1 (a) and case 2 (b).

Table 5
Iterative numbers for each component in 2D and 3D spaces.

2D:	ϕ_1	ϕ_2	ϕ_3	3D:	ϕ_1	ϕ_2	ϕ_3
Without MG:	35	34	36	Without MG:	43	46	49
With MG:	4	4	4	With MG:	4	4	4

2, respectively. From top to bottom, the snapshots correspond to different moments. Different wetting phenomena can be observed on the spherical solid substrates.

In this study, we adopt a linear multigrid algorithm (MG) equipped with a Gauss–Seidel-type relaxation method to accelerate convergence. To verify the efficiency, we perform simulations with and without an MG and count the iterative number in one time step. The 2D and 3D initial settings and parameters in case 2 are used. In particular, we use the same mesh size $h = 1/32$ in 2D and 3D spaces. The time step is set to $\Delta t = 0.01$. Table 5 lists the iterative numbers consumed in one time step for 2D and 3D simulations. The results indicate that the MG obviously accelerates the computation.

4.7. Fluid flow-coupled compound droplets in contact with solid

By utilizing the smoothed profile-type method [40] to solve the Navier–Stokes (NS) equations, a hydrodynamically coupled model can be proposed as

$$\frac{\partial \phi_l}{\partial t} + \nabla \cdot (\mathbf{u}\phi_l) = \frac{1}{Pe}\nabla \cdot ((1-\phi_0)\nabla \mu_l), \tag{26}$$

$$\mu_l = (1-\phi_0)F'(\phi_l) + \tilde{\beta}(\boldsymbol{\phi}) + \epsilon\phi_l(\phi_l - 1)|\nabla\phi_0|\cos\theta_l/\sqrt{2} - \epsilon^2\nabla\cdot((1-\phi_0)\nabla\phi_l),\ l = 1,2,3, \tag{27}$$

$$\rho^*\left(\frac{\partial \mathbf{u}}{\partial t} + \mathbf{u}\cdot\nabla\mathbf{u}\right) = -\nabla p + \frac{1}{Re}\Delta\mathbf{u} + \mathbf{SF} + (\rho(\boldsymbol{\phi}) - \rho^*)\mathbf{g} + \frac{\phi_0}{\kappa}(\mathbf{u}_s - \mathbf{u}), \tag{28}$$

$$\nabla\cdot\mathbf{u} = 0, \tag{29}$$

where $\rho(\boldsymbol{\phi})$ and $\eta(\boldsymbol{\phi})$ are determined by ϕ_l, Pe is the Peclet number, Re is the Reynolds number, $\mathbf{SF}$ is the surface tension [24], $\kappa > 0$ is the permeability, $\mathbf{u}_s$ is the velocity of the solid, ρ^* is the background density, and $\mathbf{g} = (0, -g)$ is the gravi-

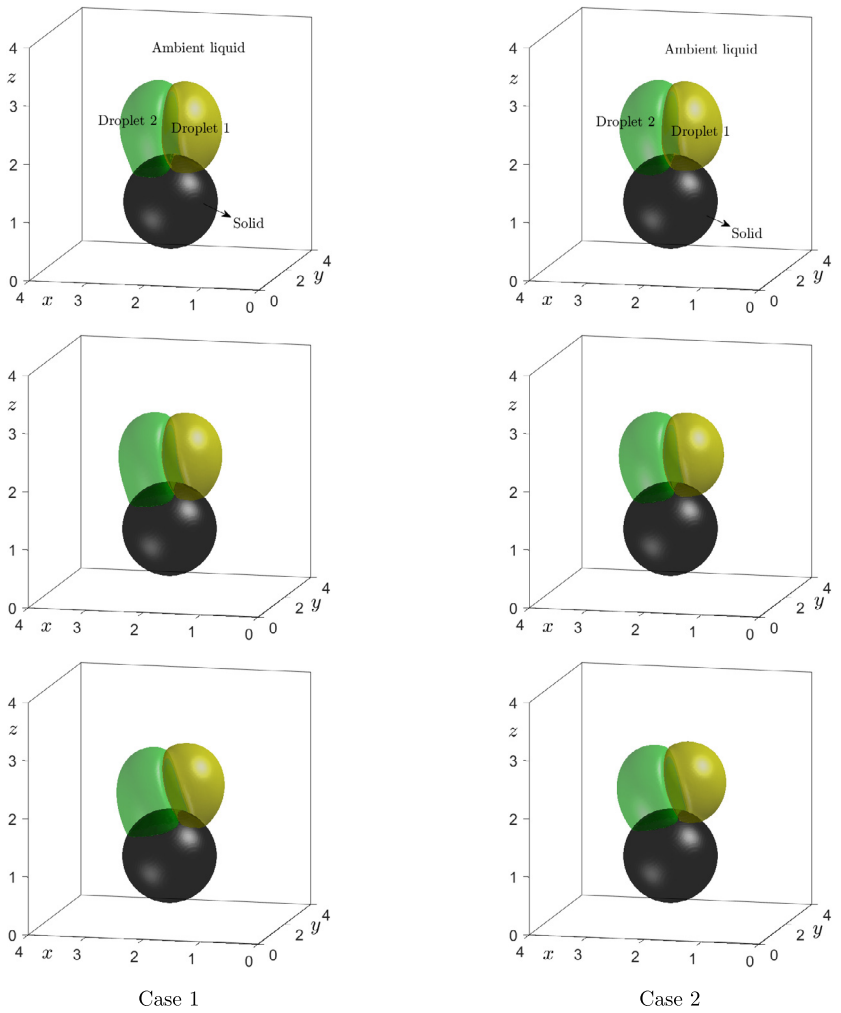

Fig. 11. Compound droplets on a spherical solid substrate in 3D space. The left and right columns correspond to cases 1 and 2. From the top to bottom, the results are at $t = 3.2$, 11.2, and 27.2.

tational acceleration. We can observe that the entire system can be directly solved on Eulerian grids. In actual application, Bergmann et al. [41] suggested that κ should take a sufficiently small value. For the purpose of numerical stability, we consider a prediction-correction strategy to split Eq. (28) into two sub-problems. In the first step, we calculate the velocity field in the absence of the last term in Eq. (28) and then we correct the velocity field in solid phase by solving an ordinary differential equation (ODE) including the last term in Eq. (28). To obtain approximate results, we can correct the velocity field using a cut-off approach similar to the augmented projection method proposed by Kim [42]. To discretize the NS equations in time, we adopt the BDF2 type scheme, see [43,44] and references therein for the implementations.

In the first case, we consider falling compound droplets that are initially in contact with a solid fibre on $\Omega = (0, 2) \times (0, 2)$. Along x-direction, all variables are periodic. On the top and bottom boundaries, homogeneous Neumann and no-slip boundary conditions are used for the phase-field function and velocities, respectively. The initial settings are shown in the left subfigure of the first row of Fig. 12. We let $\Delta t = 0.01$, $\epsilon = 0.0056$, $Re = 30$, $Pe = 1$, $\theta_{13} = 120°$, $\theta_{23} = 69.295°$, $\theta_{12} = 135°$, $\rho_1 = \rho_2 = 1.6$, $\rho_3 = 1$, and $g = 1$. As shown in Fig. 12, the compound droplets descend under the effect of buoyancy force. Owing to the different wetting conditions, droplet 1 gradually separates from the solid fibre, whereas part of droplet 2 still attaches to the fibre after the appearance of pinch-off.

In the second case, we simulate the shear flow-driven deformation of the compound droplets on a solid substrate. The full domain is set to $\Omega = (0, 4) \times (0, 2)$. The solid phase is located at $y = 0.15$. The initial settings for the compound droplets are shown in the top row of Fig. 13. In the computation, the top wall moves at a constant horizontal velocity $U = 1$. The initial velocity field is $\mathbf{u}(x, y, 0) = (u_0, 0)$, where $u_0 = Uy/2$. The periodic boundary condition is used on the left and right boundaries. Here, we use $Re = 20$, $Pe = 1$, $\Delta t = 0.005$, $\epsilon = 0.0066$, $\theta_{13} = 120°$, $\theta_{23} = 60°$, and $\theta_{12} = 135°$. The densities of all liquid components are equal and the buoyancy force is neglected. As shown in Fig. 13, the droplet 1 moves to the upper position of the droplet 2 after the early deformation, and then moves to the downstream side of the droplet 2.

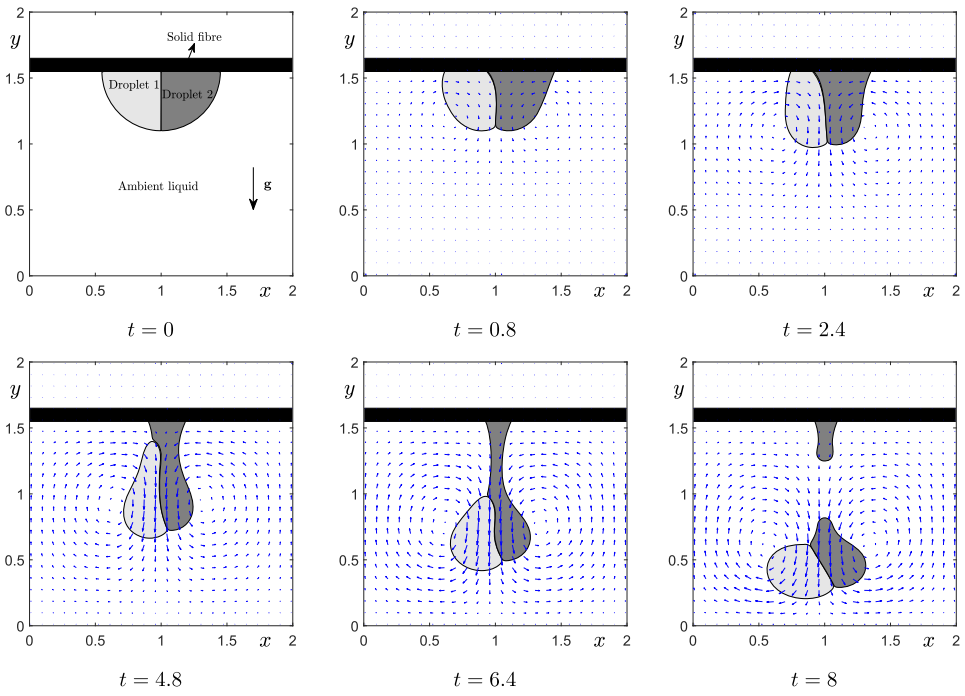

Fig. 12. Falling compound droplets. Under each figure, the computational moment is shown. The blue arrows represent the direction of velocity. (For interpretation of the colors in the figure(s), the reader is referred to the web version of this article.)

5. Discussions

Based on the equilibrium Young's equality, the proposed diffuse-interface model describes the contact angle dynamics of compound droplets in contact with a solid substrate. The motion of compound droplets near solid wall is governed by the fluid flow and diffusion-driven dynamics at the interface. A similar idea can be found in [22,24,45]. For a dynamic process that is not close to equilibrium, some researchers have developed a more accurate model with a moving contact line. Qian et al. [46] investigated molecular scale contact line dynamics with fluid flows. Based on the phase-field model, Gao and Wang [47] presented an efficient scheme and simulated flow-coupled droplets in contact with a solid. To perform a comparison, we consider a simulation similar to that in [48]. The initial droplet with a radius $R = 2$ is located at the center position of the bottom boundary. The initial velocity is zero, and the solid phase is located at $y = 0.1$, $h = 1/32$, and $\Delta t = 0.25h$. By setting one fluid phase to zero, the proposed model becomes a phase-field method for two-phase flows in irregular domains [49]. Here, the contact angle $\theta = 150°$ is constant. Fig. 14(a) displays a snapshot of the spreading droplet in [48]. The left and right columns in Fig. 14(b) show the present simulations of the two-phase profile and velocity field, respectively. Although the results are qualitatively similar, a small difference near the fluid-solid interface can be observed. It is noteworthy that the moving contact line model [46–48] is more accurate for problems in a non-equilibrium state. In a future study, we will extend the present model to better fit the dynamic process that is not close to equilibrium.

6. Concluding remarks

Here, we developed a novel diffuse-interface model to describe compound droplets in contact with a solid. The solid was represented by the fixed phase of a four-component CH system. Based on Young's equality, the equilibrium profile of the diffuse interface, and the horizontal force balance relation, a correction term reflecting the contact line dynamics for each liquid phase was derived. In the implementation, the proposed model was directly discretized on Eulerian grids using the FDM, and no artificial treatments were introduced on the liquid-solid boundary. To maintain efficiency and obtain second-order accuracy in time, we designed a linear, decoupled, and stabilized scheme based on BDF2. Various computational experiments were performed to validate the accuracy and capability of the proposed method. In future work, we will develop an efficient and practical method for handling multiple heat fluid-coupled droplets with large density and viscosity ratios [50–53] and surfactant-laden fluids [54–56] in complex geometries.

CRediT authorship contribution statement

Junxiang Yang: Formal analysis, Investigation, Methodology, Software, Supervision, Validation, Visualization, Writing – original draft, Writing – review & editing. **Yibao Li:** Investigation, Methodology, Software, Supervision, Validation, Visualiza-

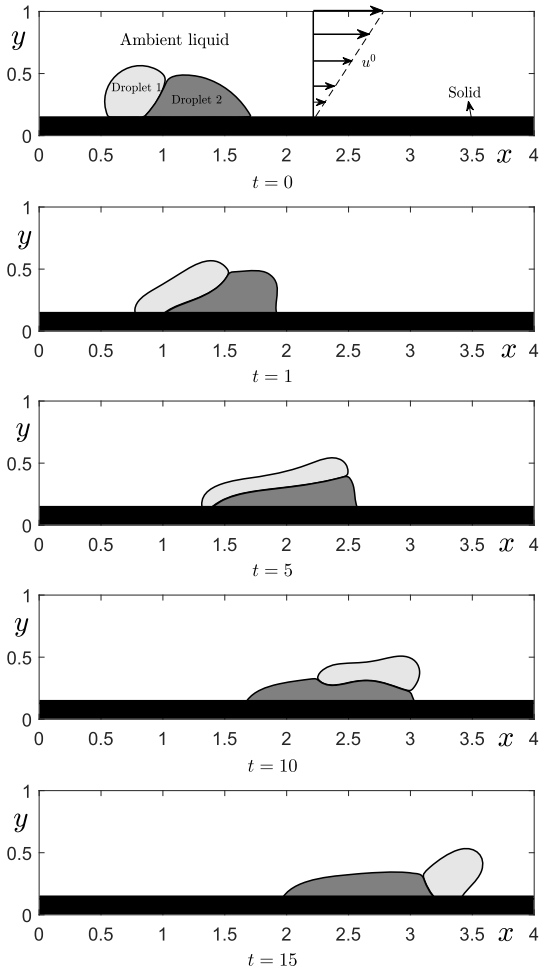

Fig. 13. Shear flow-driven deformation of compound droplets on a flat solid substrate. The computational moments are shown under each figure.

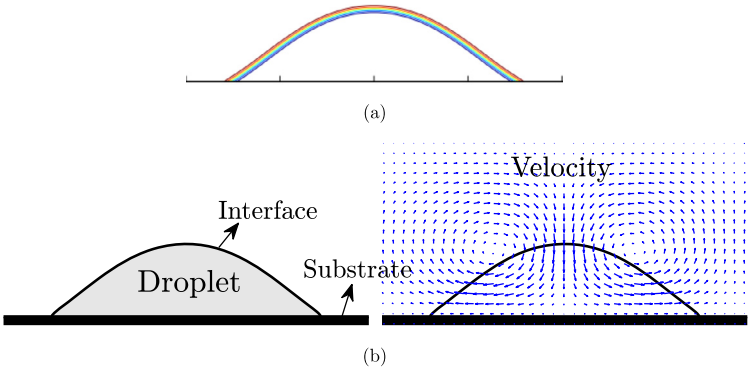

Fig. 14. Comparison study of a spreading droplet on a flat substrate. Here, (a) is the previous simulation which is adapted from [48] with the permission of Elsevier Science; (b) shows the present simulation.

tion. **Junseok Kim:** Formal analysis, Investigation, Methodology, Software, Supervision, Validation, Visualization, Writing – original draft, Writing – review & editing.

Declaration of competing interest

The authors declare that they have no known competing financial interests or personal relationships that could have appeared to influence the work reported in this paper.

Data availability

Data will be made available on request.

Acknowledgement

J. Yang is supported by the National Natural Science Foundation of China (No. 12201657), the China Postdoctoral Science Foundation (No. 2022M713639), and the 2022 International Postdoctoral Exchange Fellowship Program (Talent-Introduction Program) (No. YJ20220221). Y. Li is supported by the National Natural Science Foundation of China (No. 12271430). The corresponding author (J.S. Kim) was supported by the National Research Foundation of Korea (NRF) grant funded by the Korea government (MSIT) (No. 2022R1A2C1003844). The authors thank the anonymous reviewers for constructive comments on the revision.

Appendix A

By adding Eq. (8) into the right-hand side of Eq. (2), we have

$$\mu_l = F'(\phi_l) \underbrace{-\epsilon^2 \Delta \phi_l}_{\text{I}} + \beta(\boldsymbol{\phi}) \underbrace{+\epsilon^2 \nabla \phi_0 \cdot \nabla \phi_l}_{\text{II}} + \epsilon \phi_l(\phi_l - 1)|\nabla \phi_0| \cos\tilde{\theta}/\sqrt{2}. \tag{30}$$

Using the chain rule, the combination of terms I and II equals to $-\epsilon^2 \nabla \cdot ((1-\phi_0)\nabla\phi_l) - \epsilon^2 \phi_0 \Delta \phi_l$. Subsequently, we obtain the equivalent form as follows:

$$\mu_l = F'(\phi_l) + \hat{\beta}(\boldsymbol{\phi}) + \epsilon \phi_l(\phi_l - 1)|\nabla \phi_0| \cos\tilde{\theta}/\sqrt{2} - \epsilon^2 \nabla \cdot ((1-\phi_0)\nabla\phi_l) - \epsilon^2 \phi_0 \Delta \phi_l. \tag{31}$$

For fluid phases, $\phi_0 = 0$. This indicates that aforementioned equation and Eq. (13) are equivalent in the regions occupied by fluids. On the fluid-solid interface, the last term of the above equation approximates to zero as $\phi_0 \to 0$. Furthermore, the last term contributes less to the wetting dynamics because it does not include the contact angle θ. For convenience, we neglect the effect of the last term on the fluid-solid interface and derive Eq. (13).

Appendix B

Using the constraint $\phi_0 + \phi_1 + \phi_2 + \phi_3 = 1$, we have $\frac{\partial \psi}{\partial t} = 0$ and $\psi = \sum_{l=0}^{3} \phi_l$. Because ϕ_0 is fixed in the computation, we get

$$0 = \frac{\partial(\phi_1 + \phi_2 + \phi_3)}{\partial t} = M\nabla \cdot \left((1-\phi_0)\nabla \sum_{l=1}^{3} \mu_l \right). \tag{32}$$

Here, we can simply set $\sum_{l=1}^{3} \mu_l = 0$ to suppress the time evolution of $\sum_{l=1}^{3} \phi_l$. In the aforementioned equation, $1-\phi_0$ is used to suppress the evolutions of fluids in solid. From $\sum_{l=1}^{3} \mu_l = 0$, we have

$$\sum_{l=1}^{3} (1-\phi_0) F'(\phi_l) + 3\tilde{\beta}(\boldsymbol{\phi}) + \sum_{l=1}^{3} \left[\epsilon \phi_l(\phi_l - 1)|\nabla \phi_0| \cos\tilde{\theta}/\sqrt{2} \right] - \epsilon^2 \nabla \cdot \left[(1-\phi_0)\nabla \left(\sum_{l=1}^{3} \phi_l \right) \right] = 0. \tag{33}$$

In fluid region, we have $\sum_{l=1}^{3} \phi_l = 1$, the last term on the left-hand side of Eq. (33) can be neglected. Thus, we obtain the expression of $\tilde{\beta}(\boldsymbol{\phi})$ as

$$\tilde{\beta}(\boldsymbol{\phi}) = -\frac{1}{3} \left[\sum_{l=1}^{3} \left((1-\phi_0) F'(\phi_l) + \epsilon \phi_l(\phi_l - 1)|\nabla \phi_0| \cos\theta_l/\sqrt{2} \right) \right].$$

References

[1] C.Cui.J. Liu, Y. Mo, S. Zhai, An effective operator splitting scheme for two-dimensional conservative nonlocal Allen–Cahn equation, Appl. Math. Lett. 130 (2022) 108016.
[2] H.G. Lee, J. Shin, J-Y. Lee, Energy quadratization Runge–Kutta scheme for the conservative Allen–Cahn equation with a nonlocal Lagrange multiplier, Appl. Math. Lett. 132 (2022) 108161.
[3] H-R. Liu, C.S. Ng, K.L. Chong, D. Lohse, R. Verzicco, An efficient phase-field method for turbulent multiphase flows, J. Comput. Phys. 446 (2021) 110659.
[4] M. Sohaib, A. Shah, Fully decoupled pressure projection scheme for the numerical solution of diffuse interface model of two-phase flow, Commun. Nonlinear Sci. Numer. Simul. 112 (2022) 106547.
[5] Y. Qin, H. Huang, Y. Zhu, C. Liu, S. Xu, A phase field model for mass transport with semi-permeable interfaces, J. Comput. Phys. 464 (2022) 111334.
[6] Z. Guo, P. Lin, J. Lowengrub, S.M. Wise, Mass conservative and energy stable finite difference methods for the quasi-incompressible Navier–Stokes–Cahn–Hilliard system: primitive variable and projection-type schemes, Comput. Methods Appl. Mech. Eng. 326 (2017) 144–174.

[7] J-J. Huang, L. Zhang, Simplified method for wetting on curved boundaries in conservative phase-field lattice-Boltzmann simulation of two-phase flows with large density ratios, Phys. Fluids 34 (2022) 082101.
[8] N. Valizadeh, T. Rabczuk, Isogeometric analysis of hydrodynamics of vesicles using a monolithic phase-field approach, Comput. Methods Appl. Mech. Eng. 388 (2022) 114191.
[9] M. Ashour, N. Valizadeh, T. Rabczuk, Isogeometric analysis for a phase-field constrained optimization problem of morphological evolution of vesicles in electrical fields, Comput. Methods Appl. Mech. Eng. 377 (2021) 113669.
[10] J. Yang, Y. Li, J. Kim, Totally decoupled implicit-explicit linear scheme with corrected energy dissipation law for the phase-field fluid vesicle model, Comput. Methods Appl. Mech. Eng. 399 (2022) 115330.
[11] Q. Li, N. Cui, S. Zheng, L. Mei, A new Allen–Cahn type two-model phase-field crystal model for fcc ordering and its numerical approximation, Appl. Math. Lett. 132 (2022) 108211.
[12] H.G. Lee, An energy stable method for the Swift–Hohenberg equation with quadratic-cubic nonlinearity, Comput. Methods Appl. Mech. Eng. 343 (2019) 40–51.
[13] W. Chen, C. Wang, S. Wang, X. Wang, S.M. Wise, Energy stable numerical schemes for ternary Cahn–Hilliard system, J. Sci. Comput. 84 (2020) 27.
[14] M. Yuan, W. Chen, C. Wang, S. Wise, Z. Zhang, An energy stable finite element scheme for the three-component Cahn–Hilliard-type model for macromolecular microsphere composite hydrogels, J. Sci. Comput. 87 (2021) 78.
[15] S-T. Zhang, J-X. Zhou, H-W. Xiao, X-D. Niu, H. Wei, A. Khan, D-C. Li, H. Yamaguchi, A generalized conservative phase-field simplified lattice Boltzmann method for miscible and immiscible ternary flows with large density ratio, Int. J. Multiph. Flow 149 (2022) 103978.
[16] H. Liang, J. Xu, J. Chen, Z. Chai, B. Shi, Lattice Boltzmann modeling of wall-bounded ternary fluid flows, Appl. Math. Model. 73 (2019) 487–513.
[17] H. Liang, B.C. Shi, Z.H. Chai, Lattice Boltzmann modeling of three-phase incompressible flows, Phys. Rev. E 93 (2016) 013308.
[18] S. Zhou, Y.M. Xie, Numerical simulation of three-dimensional multicomponent Cahn–Hilliard systems, Int. J. Mech. Sci. 198 (2021) 106349.
[19] J. Kim, A generalized continuous surface tension force formulation for phase-field models for immiscible multi-component fluid flows, Comput. Methods Appl. Mech. Eng. 198 (2009) 3105–3122.
[20] H.G. Lee, J. Kim, An efficient numerical method for simulating multiphase flows using a diffuse interface model, Physica A 423 (2015) 33–50.
[21] Y. Li, J-I. Choi, J. Kim, Multi-component Cahn–Hilliard system with different boundary conditions in complex domains, J. Comput. Phys. 323 (2016) 1–16.
[22] H-L. Li, H-R. Liu, H. Ding, A fully 3D simulation of fluid-structure interaction with dynamic wetting and contact angle hysteresis, J. Comput. Phys. 420 (1) (2020) 109709.
[23] J. Yang, J. Wang, J. Kim, Energy-stable method for the Cahn–Hilliard equation in arbitrary domains, Int. J. Mech. Sci. 228 (2022) 107489.
[24] C-Y. Zhang, H. Ding, P. Gao, Y-L. Wu, Diffuse interface simulation of ternary fluids in contact with solid, J. Comput. Phys. 309 (2016) 37–51.
[25] J-J. Huang, Hybrid lattice-Boltzmann finite difference simulation of ternary fluids near immersed solid objects of general shapes, Phys. Fluids 33 (2021) 072105.
[26] Z. Huang, G. Lin, A.M. Ardekani, Implementing contact angle boundary conditions for second-order Phase-Filed models of wall-bounded multiphase flows, J. Comput. Phys. 471 (2022) 111619.
[27] D. Jeong, J. Yang, J. Kim, A practical and efficient numercial method for the Cahn–Hilliard equation in complex domains, Commun. Nonlinear Sci. Numer. Simul. 73 (2019) 217–228.
[28] S. Aland, J. Lowengrub, A. Voigt, Two-phase flow in complex geometries: a diffuse domain approach, Comput. Model. Eng. Sci. 57 (1) (2010) 77–106.
[29] J. Shin, S. Kim, D. Lee, J. Kim, A parallel multigrid method for the Cahn–Hilliard equation, Comput. Mater. Sci. 71 (2013) 89–96.
[30] U. Trottenberg, C. Oosterlee, A. Schüller, Multigrid, Academic Press, New York, 2001.
[31] J. Kim, K. Kang, J. Lowengrub, Conservative multigrid methods for Cahn–Hilliard fluids, J. Comput. Phys. 193 (2) (2004) 511–543.
[32] J. Yang, J. Kim, An unconditionally stable second-order accurate method for systems of Cahn–Hilliard equations, Commun. Nonlinear Sci. Numer. Simul. 87 (2020) 105276.
[33] S. Wise, J. Kim, J. Lowengrub, Solving the regularized, strongly anisotropic Cahn–Hilliard equation by an adaptive nonlinear multigrid method, J. Comput. Phys. 226 (2007) 414–446.
[34] J. Shen, X. Yang, Numerical approximations of Allen–Cahn and Cahn–Hilliard equations, Discrete Contin. Dyn. Syst., Ser. A 28 (2010) 1669–1691.
[35] J. Yang, J. Kim, Numerical approximation of the square phase-field crystal dynamics on the three-dimensional objects, J. Comput. Phys. 471 (2022) 111652.
[36] X. Yang, Efficient and energy stable scheme for the hydrodynamically coupled three components Cahn–Hilliard phase-field model using the stabilized-Invariant Energy Quadratization (S-IEQ) Approach, J. Comput. Phys. 438 (2021) 110342.
[37] C. Chen, X. Yang, A second-order time accurate and fully-decoupled numerical scheme of the Darcy–Newtonian–Nematic model for two-phase complex fluids confined in the Hele–Shaw cell, J. Comput. Phys. 456 (2022) 111026.
[38] J. Yang, J. Kim, A variant of stabilized-scalar auxiliary variable (S-SAV) approach for a modified phase-field surfactant model, Comput. Phys. Commun. 261 (2021) 107825.
[39] Q. Ye, Z. Ouyang, C. Chen, X. Yang, Efficient decoupled second-order numerical scheme for the flow-coupled Cahn–Hilliard phase-field model of two-phase flows, J. Comput. Appl. Math. 405 (2022) 113875.
[40] Y. Hu, D. Li, S. Shu, X. Niu, An efficient smoothed profile-lattice Boltzmann method for the simulation of forced and natural convection flows in complex geometries, Int. Commun. Heat Mass Transf. 68 (2015) 188–199.
[41] M. Bergmann, J. Hovnanian, A. Iollo, An accurate cartesian method for incompressible flows with moving boundaries, Commun. Comput. Phys. 15 (2014) 1266–1290.
[42] J. Kim, An augmented projection method for the incompressible Navier–Stokes equations in arbitrary domains, Int. J. Comput. Methods 2 (2) (2005) 1–12.
[43] J. Yang, J. Kim, Numerical study of the ternary Cahn–Hilliard fluids by using an efficient modified scalar auxiliary variable approach, Commun. Nonlinear Sci. Numer. Simul. 102 (2021) 105923.
[44] J. Yang, J. Wang, Z. Tan, J. Kim, Efficient IMEX and consistently energy-stable methods of diffuse-interface models for incompressible three-component flows, Comput. Phys. Commun. 282 (2023) 108558.
[45] H-R. Liu, P. Gao, H. Ding, Fluid-structure interaction involving dynamic wetting: 2D modeling and simulations, J. Comput. Phys. 348 (2017) 45–65.
[46] T. Qian, X-P. Wang, P. Sheng, Molecular scale contact line hydrodynamics of immiscible flows, Phys. Rev. E 68 (1) (2003) 016306.
[47] M. Gao, X-P. Wang, An efficient scheme for a phase field model for the moving contact line problem with variable density and viscosity, J. Comput. Phys. 272 (2014) 704–718.
[48] J. Shen, X. Yang, H. Yu, Efficient energy stable numerical schemes for a phase field moving contact line model, J. Comput. Phys. 284 (2015) 617–630.
[49] J. Yang, J. Kim, A phase-field method for two-phase fluid flow in arbitrary domains, Comput. Math. Appl. 79 (2020) 1857–1874.
[50] X. Pan, K-H. Kim, J-I. Choi, Monolithic projection-based method with staggered time discretization for solving non-Oberbeck–Boussinesq natural convection flows, J. Comput. Phys. 463 (2022) 111238.
[51] G. Fu, D. Han, A linear second-order in time unconditionally energy stable finite element scheme for a Cahn–Hilliard phase-field model for two-phase incompressible flow of variable densities, Comput. Methods Appl. Mech. Eng. 387 (2021) 114186.

[52] L. Luo, X-P. Wang, X-C. Cai, An efficient finite element method for simulation of droplet spreading on a topologically rough surface, J. Comput. Phys. 349 (2017) 233–252.
[53] M.E. Haddad, G. Tierra, A thermodynamically consistent model for two-phase incompressible flows with different densities. Derivation and efficient energy-stable numerical schemes, Comput. Methods Appl. Mech. Eng. 389 (2022) 114328.
[54] G. Zhu, J. Kou, J. Yao, A. Li, S. Sun, A phase-field moving contact line model with soluble surfactants, J. Comput. Phys. 405 (2020) 109170.
[55] G. Zhu, J. Kou, B. Yao, Y-s Wu, J. Yao, S. Sun, Thermodynamically consistent modelling of two-phase flows with moving contact line and soluble surfactants, J. Fluid Mech. 879 (2019) 327–359.
[56] J. Yang, Z. Tan, J. Kim, Linear and fully decoupled scheme for a hydrodynamics coupled phase-field surfactant system based on a multiple auxiliary variables approach, J. Comput. Phys. 452 (2022) 110909.